Computational Materials Science 169 (2019) 109088

Contents lists available at ScienceDirect

Computational Materials Science

journal homepage: www.elsevier.com/locate/commatsci

Effect of magnetic ordering on the spinodal decomposition of the Fe-Cr system: A GPU-accelerated phase-field study

Jeonghwan Lee, Kunok Chang*

Department of Nuclear Engineering, Kyung Hee University, Yong-in City, Republic of Korea

ARTICLE INFO

Keywords:
Fe-Cr
Spinodal decomposition
Phase-field modeling

ABSTRACT

This study aims to investigate the effect of magnetic ordering on spinodal decomposition behavior in the Fe-Cr system using graphics processing unit(GPU) parallelization. We modify the CALPHAD-type free energy to remove its critical behavior near the paramagnetic-ferromagnetic transition. We solve the Cahn-Hilliard equation using a semi-implicit Fourier spectral method, parallelizing the code to run on a GPU via compute unified device architecture and OpenMP. We find that the GPU parallelization gives better performance than that of OpenMP when using fast Fourier transforms to solve the Cahn-Hilliard equation. We conduct nine sets of simulations to examine the effect of magnetic ordering, and we found that it alters the interfacial energy between Cr-rich and Cr-depleted phases, equilibrium concentrations, and energy barrier for phase transformations. We apply a phase-field method to examine in detail how these changes affect the microstructural evolution, quantitatively evaluating the microstructures obtained in terms of the precipitate number density, average phase area, and phase boundary density along certain auxiliary lines to analyze the effects of magnetic ordering.

1. Introduction

Several previous studies have shown that the α' phase plays an important role in the hardening/embrittlement of ferritic steels [1–3]; therefore, understanding the spinodal decomposition behavior of the Fe-Cr system has been an important topic in studying the integrity of structural materials [1–9]. The free energy of the Fe-Cr system can be assessed quantitatively using CALPHAD approach [10], and has been used as an input for the phase-field modeling of spinodal decomposition in the Fe-Cr system [5–7].

Herein, we analyze the effect of magnetic ordering on the microstructural evolution of the Fe-Cr system using a graphics processing unit (GPU)-accelerated phase-field method. Since this system can undergo magnetic ordering transitions [10] depending on the Cr composition at $T = 700$ K, we quantify the effect of magnetic ordering on a single crystal using the phase-field method. The Fe-Cr system is considered to be a prototype for various ferritic/martensitic steel alloys; therefore, examining the magnetic ordering's effect on its microstructural evolution can provide a guide line for alloy design from the viewpoint of microstructural optimization.

In addition, we also consider two different computational technique. Since the quantitative prediction of the real material system is highly computationally expensive, we have implement a parallel computing scheme based on the compute unified device architecture (CUDA) to improve computational efficiency [11], comparing it with parallelized code using CUDA and OpenMP [12] when solving the Cahn-Hilliard diffusion equation [13] using a semi-implicit spectral method [14].

Although CUDA has previously been applied to the phase-field method, it was used to create an explicit solver [15,16]. Herein, we instead use it to implement a semi-implicit spectral method and compare the performance of OpenMP- and CUDA-accelerated code. Results will help to guide any researchers aiming to solve the Cahn-Hilliard equation using fast Fourier transform.

2. CALPHAD-based phase-field method

2.1. Semi-implicit Fourier spectral method

We simulate the evolution of the Cr concentration field by solving the following Cahn-Hilliard equation [17]:

$$\frac{\partial c(\mathbf{r}, t)}{\partial t} = V_m^2 \nabla \cdot \left[M(\mathbf{r}, t) \cdot \nabla \left(\frac{\delta F(\mathbf{r}, t)}{\delta c} \right) \right] \tag{1}$$

$$F(\mathbf{r}, t) = \int_V \{ \frac{1}{V_m} \left[f(c) + \frac{1}{2} \kappa (\nabla c)^2 \right] \} dV \tag{2}$$

* Corresponding author.
E-mail address: kunok.chang@khu.ac.kr (K. Chang).

https://doi.org/10.1016/j.commatsci.2019.109088
Received 29 April 2019; Received in revised form 15 June 2019; Accepted 15 June 2019
Available online 01 July 2019
0927-0256/ © 2019 Elsevier B.V. All rights reserved.

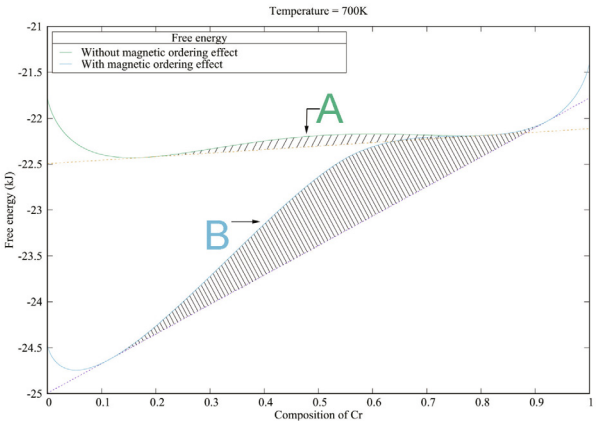

(a) Plot of free energy with respect to the whole Cr concentration range

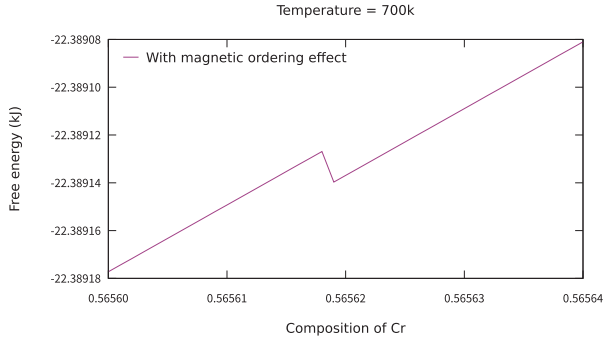

(b) Plot of free energy with respect to the Cr concentration in the vicinity of $c = 0.5652$

Fig. 1. Free energy curves for the Fe-Cr system at 700 K with and without considering magnetic ordering effects. The equilibrium Cr concentrations without magnetic ordering effects are $c_{cr} = 0.18$ and 0.82, and considering such effects changes these to $c_{cr} = 0.11$ and 0.92.

where c is the Cr concentration, κ is the gradient energy coefficient, and $F(\mathbf{r}, t)$ and $f(c)$ are the system's molar free energy and molar chemical free energy, respectively. $f(c)$ is discussed in the following section.

The molar free energy $F(r, t)$ in Eq. (1) is given by Eq. (2), whereas the mobility $M(r, t)$ is given by Darken's equation [18,19]:

$$M(\mathbf{r}, t) = \frac{1}{V_m}[cM_{Fe} + (1-c)M_{Cr}]c(1-c) \tag{3}$$

where M_{Fe} and M_{Cr} are the mobilities of the Fe and Cr atom, respectively. The solutes' diffusivities are given (in units of m^2/s) by [7]

$$D_{Fe} = 1.0 \times 10^{-4}\exp\left(-\frac{294(kJ/mol)}{RT}\right) \tag{4}$$

$$D_{Cr} = 2.0 \times 10^{-5}\exp\left(-\frac{308(kJ/mol)}{RT}\right) \tag{5}$$

and the gradient coefficient κ is given by [13]

$$\kappa = \frac{1}{6}r_0^2 L_{FeCr} \tag{6}$$

where r_0 is the lattice parameter and L_{FeCr} is the regular solution interaction parameter [13].

To efficiently solve Eq. (1), we implemented a semi-implicit Fourier spectral scheme [14] by expanding the formula as follows. For the ease of convenience, we introduced

$$\phi(\mathbf{r}, t) = [cM_{Fe} + (1-c)M_{Cr}]c(1-c) \tag{7}$$

and then rearranged Eq. (1) as

$$\frac{\partial c(\mathbf{r}, t)}{\partial t} = \nabla\cdot\phi(\mathbf{r}, t)\nabla\left[\frac{\delta f(c)}{\delta c} - \kappa\nabla^2 c(\mathbf{r}, t)\right] \tag{8}$$

$$\frac{\partial \tilde{c}(\mathbf{k}, t)}{\partial t} = ik\cdot\{\phi(\mathbf{r}, t)[ik'(\{\frac{\delta f(c)}{\delta c}\}'_k + \kappa k'^2\tilde{c}(\mathbf{k}', t))]_r\}_k \tag{9}$$

where $\mathbf{k} = (k_l, k_2)$ is the reciprocal vector in the Fourier space of magnitude $k = \sqrt{k_1^2 + k_2^2}$ and $\tilde{c}(\mathbf{k}, t)$ and $\{\frac{\delta f}{\delta c}\}'_k$ are the Fourier transforms of $c(r, t)$ and $\frac{\delta f}{\delta c}$, respectively. Then, we applied an explicit Euler Fourier spectral treatment to this equation, yielding

$$\frac{\partial \tilde{c}^{n+1}(k, t) - \tilde{c}^n(k, t)}{\Delta t} = ik\cdot\left\{\phi(\mathbf{r}, t)\left[ik'\left(\left\{\frac{\delta f(c)}{\delta c}\right\}^n_{k'} + \kappa k'^2\tilde{c}^n(k', t)\right)\right]_r\right\}_k \tag{10}$$

so

$$\tilde{c}^{n+1}(k, t) = \tilde{c}^n(k, t) + \frac{\Delta tik\cdot\{\phi(\mathbf{r}, t) \times \left[ik'\left(\left\{\frac{\delta f(c)}{\delta c}\right\}^n_{k'} + \kappa k'^2\tilde{c}^n(k', t)\right)\right]_r\}_k}{(1 + A\Delta t\kappa k^4)} \tag{11}$$

where

$$A = \frac{1}{2}[max(\phi(\mathbf{r}, t)) + min(\phi(\mathbf{r}, t))]. \tag{12}$$

2.2. Modified CALPHAD-type free energy

The molar chemical free energy $f(c)$ in Eq. (2) is given by [20]

$$f(c) = (1-c)G^0_{Fe} + cG^0_{Cr} + L_{FeCr}c(1-c) + RT(c\ln c + (1-c)\ln(1-c)] + G_m(J/mol) \tag{13}$$

where G^0_{Fe} and G^0_{Cr} are the molar Gibbs free energies for pure elemental Fe and Cr, respectively, L_{FeCr} is the interaction parameter between Fe

and Cr, R (= $8.314 J/mol{\cdot}K$) is the gas constant, T is the system's absolute temperature, which is 700 K herein, and G_m is the molar Gibbs free energy of the magnetic ordering effect [10]. These were calculated as follows:

$$
\begin{aligned}
G^0_{Fe} &= +1225.7 + 124.134 \times T - 23.5143 \times T \times \ln T - 0.00439752 \times T^2 \\
&\quad - 5.89269 \times 10^{-8} \times T^3 + 77358.5 \times T^{-1} \\
G^0_{Cr} &= -8856.94 + 157.48 \times T - 26.908 \times T \times \ln T + 0.00189435 \times T^2 \\
&\quad - 1.47721 \times 10^{-6} \times T^3 + 139250 \times T^{-1} \\
L_{FeCr} &= +20500 - 9.68T \\
G_m &= RT\ln(\beta + 1)\lambda(\tau), (J/mol)
\end{aligned}
$$

where β is the atomic magnetic moment, calculated in terms the Bohr magneton as $\beta = 2.22(1 - c) - 0.008c - 0.85c(1 - c)$. The function $\lambda(\tau)$ is expressed as the following polynomial:

$$
\begin{aligned}
\lambda(\tau) = &-0.90530\tau^{-1} + 1.0 - 0.153\tau^3 - 6.8 \times 10^{-3}\tau^9 \\
&- 1.53 \times 10^{-3}\tau^{15}(\tau < 1) - 0.06417\tau^{-5} - 2.037 \times 10^{-3}\tau^{-15} \\
&- 4.278 \times 10^{-4}\tau^{-25}(\tau > 1) \qquad (14)
\end{aligned}
$$

where $\tau = T/T_c$ is critical magnetic ordering temperature given by $T_c = 1043(1 - c) - 311.5c + c(1 - c)[1650 + 550(2c - 1)]$ (in K).

Eq. (2) includes a magnetic ordering contribution to the free energy. Some previous studies have neglected magnetic ordering effects [5,9]. However, as shown in Fig. 1, the Fe-Cr system's free energy at 700 K varies substantially depending on whether or not magnetic ordering effects are included.

To investigate the effect of magnetic ordering, we performed nine sets of simulations. Herein, we neglected the G_m term in Eq. (13) when simulating microstructural evolution without such effects.

To increase the computational efficiency, we used dimensionless values herein. Specifically, our simulations used the normalized values $\mathbf{r}^* = \mathbf{r}/l$, $\nabla^* = \partial/\partial(\mathbf{r}/l)$, $t^* = tD/l^2$, $M^* = V_m RT^* M/Df^*(c) = f(c)/(RT^*)$, and $\kappa^* = \kappa/(RT^* l^2)$ with $D = 10^{-24} m^2/s$[7], $T^* = 900K$, and $l = 2.856$ Å, where is a_0 value in Eq. (6). Without magnetic ordering effects, the dimensionless κ_1^* value in Eq. (6) was 0.3057. The gradient coefficient is proportional to the area between the free energy curve and the common tangent line, such as areas A and B in Fig. 1. After evaluating areas A and B numerically, we found that the ratio of B to A was 8.1463; therefore, we used $\kappa_2^* = 2.4901$ when considering magnetic ordering effects. To evaluate the interface width for the both cases, we performed 1-D simulation of $\alpha - \alpha'$ structure. We achieved the equilibrium state, which means the concentration profile is entirely stationary and plotted the profile in Fig. 2. We can measure the interface width using the method proposed by Cahn [13]. In practice, people measure the number of grid points within the interface region more intuitively. When the equilibrium concentration profile of Cr at α phase is 0.18 and that of the α' phase is 0.82 then, we assume that when the concentration c is within the range $0.18 + (0.82 - 0.18) \times 0.1 \leqslant c < 0.82 - (0.82 - 0.18) \times 0.1$, it becomes $0.244 \leqslant c < 0.756$. We also measured the interface width of the $\alpha - \alpha'$ cases with magnetic ordering cases and we found that the interface width is consistently 3 grid points.

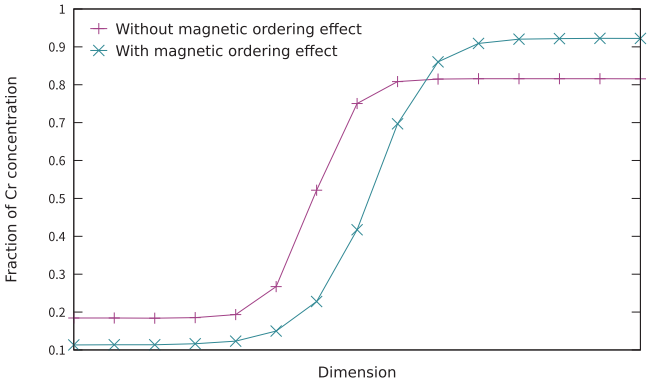

Fig. 2. Equilibrium concentration profiles of across the phase boundary with and with out magnetic ordering effect of Fe-Cr system at $T = 700K$.

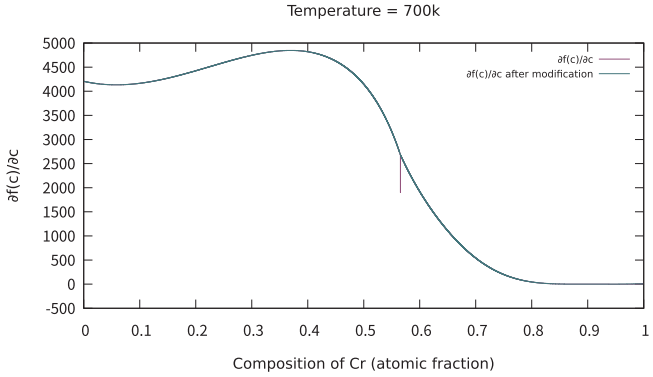

Fig. 3. Plot of $\frac{\partial f(c)}{\partial c}$ with respect to c, where c is the Cr composition (atomic fraction). The derivative of Eq. (13) was calculated using a finite difference method. We removed the steep spike in the vicinity of $c = 0.56525$ and show the modified curve in green.

After plotting the partial derivative $\frac{\partial f(c)}{\partial c}$ (Fig. 3), we found that there was a steep spike near $c = 0.56525$ due to the magnetic ordering transition from a ferromagnetic to a paramagnetic state. To improve the numerical stability, we removed this rapid change and used the modified $\frac{\partial f(c)}{\partial c}$ in Eq. (8) and later. In Fig. 1 (a), the transition was not clearly observed, therefore, we plotted higher magnified version of Fig. 1 (a) near the transition at Fig. 1 (b), we confirmed that there is also transition effect in not only first derivative, but also the free energy itself.

2.3. Performance benchmark

To improve the computational efficiency, we implemented parallelization techniques based on both OpenMP [12] and CUDA [11]. A semi-implicit Fourier spectral method, as described in the previous section, was implemented by utilizing FFTW [21] for the OpenMP code and cuFFT [22] for the CUDA code. For this benchmark, we conducted 2D spinodal decomposition simulations that accounted for magnetic ordering effects. The system was $1024\Delta x \times 1024\Delta y$ in size, and we measured the time taken to calculate 10, 000 time steps using the Linux *time* command, which gives the real elapsed time. Our workstation included an Intel i7-8700 3.2 GHz CPU and the time taken decreased with the number of CPU cores used up to 12 cores.

As depicted in Fig. 4, since i7-8700K CPU has 6 cores, the CPU shows the saturated performance when we use 6 or more threads. We compared the efficiencies of the CUDA- and OpenMP-based code on the same or a comparable computer, and the results obtained are shown in Fig. 5. We conducted these comparisons for five different numbers of dimensions, namely 128, 256, 512, 1024, and 2048. Here, a dimensionality of 128 (say) means that the system cell size was $128\Delta x \times 128\Delta y$.

As shown in Fig. 5 the computational cost of the CUDA code was around half in comparison to that of the OpenMP code in all cases, when comparing CUDA on a GPU with OpenMP on a comparably priced CPU (NVIDIA GTX-1060 GPU and Intel i7-8700 3.2 GHz CPU). However, the GTX-1060 GPU only included 6 *GB* of memory, which could clearly limit CUDA's efficiency for 3D simulations.

2.4. Simulation results and analysis

To investigate the effects of magnetic ordering on phase separation behavior, we performed nine sets of simulations shown in Table 1.

We set the initial Cr concentration using the formula

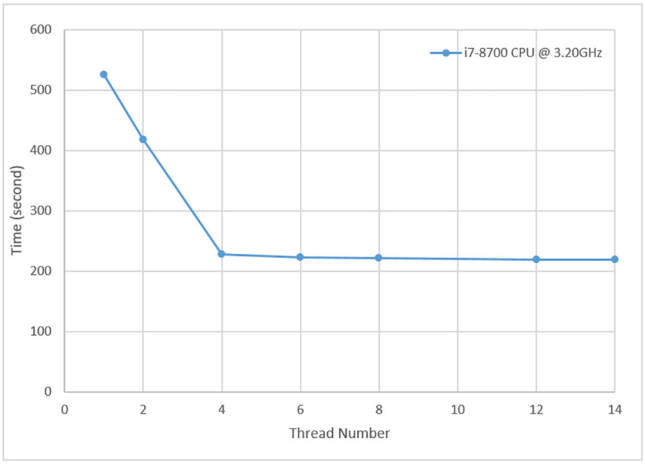

Fig. 4. Time consumption for the microstructural evolution simulation depending on number of CPU cores.

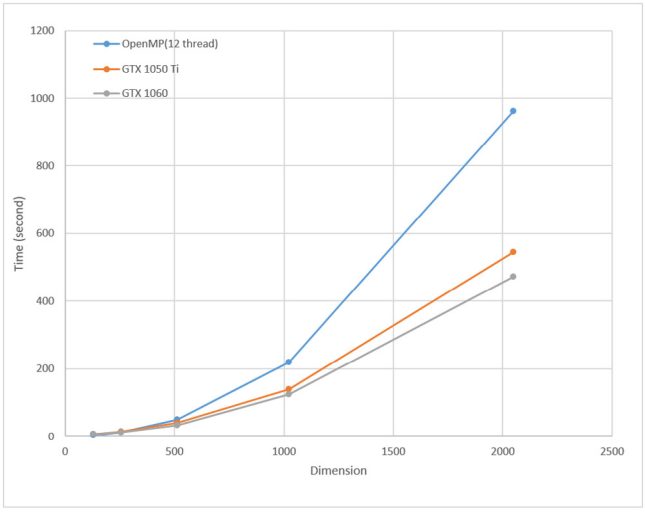

Fig. 5. Time consumption for the microstructural evolution simulation with parallelized by OpenMP (i7-8700 3.2 GHz CPU) and CUDA (GTX-1050Ti and GTX-1060).

$c(\mathbf{r}, t) = c_0 + 0.01 \times (rnd - 0.5)$ where rnd is a random number between 0 and 1, which is generated by Fortran's intrinsic random function, and c_0 is listed in the second column of Table 1.

We also set two other variables, namely the initial average concentration and α' phase fraction. Therefore, cases 1 and 2 began with identical initial states, as did cases 4 and 5 and 7 and 8. However, as shown in Fig. 1, the equilibrium concentrations of the α and α' phases changed depending on whether or not the magnetic ordering effects were considered; therefore, the α' phase fractions were different for cases 1 and 2, i.e., 0.305 and 0.316, respectively. We also conducted additional sets of simulations (cases 3, 6, and 9) with the same α' phase fractions as the corresponding cases without magnetic ordering effects (cases 1, 4, and 7). The simulation cell size was $0.292\,\mu m \times 0.292\,\mu m$, where $0.292\,\mu m$ was 1024 grid points in these simulations.

Since the critical size of stable nuclei is proportional to the interfacial energy between the matrix and precipitate [23], it is more than eight times larger when the magnetic ordering effects are included; for example, in Fig. 1, the interfacial energy is 8.1463 times higher when magnetic ordering effects are included. This means that the incubation time for nucleation is much longer in the presence of magnetic ordering effects, such as in cases 2 and 3 in comparison with case 1. Since the nucleation barrier is also significantly higher, we see noticeably less

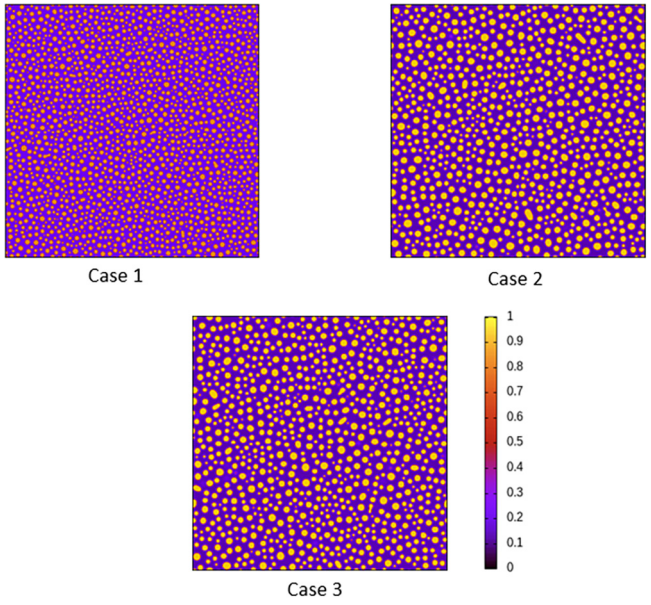

Fig. 6. Plots of the Cr concentration at $t = 8156.7s$ (1.0×10^6 time steps) for cases 1–3 in Table 1. Herein, there are 21770, 10242, and 10709 α' precipitates per μm^2, respectively, and the average precipitate areas are 14.01, 30.81, and 28.48 nm^2.

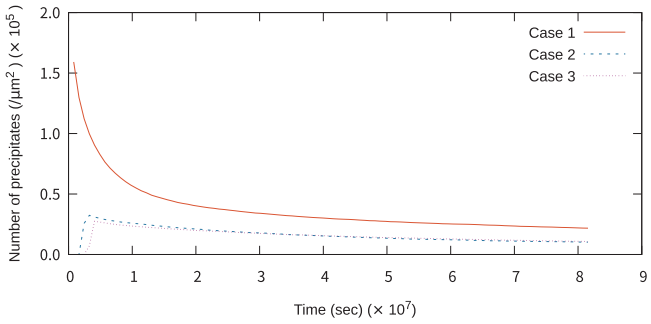

Fig. 7. Plots of the number density of α' precipitates per unit area (μm^2) for cases 1–3 in Table 1.

Table 1
Nine sets of simulations for various average initial Cr concentrations with and without considering the magnetic ordering effects. Since the α' phase fraction varied slightly over time, we measured the value at $t = 8156.7s$.

Case	Initial average concentration	Magnetic effect	Fraction of α' phase	Gradient coefficient
1	0.385	No	0.305	0.3057
2	0.385	Yes	0.316	2.4901
3	0.377	Yes	0.305	2.4901
4	0.400	No	0.330	0.3057
5	0.400	Yes	0.335	2.4901
6	0.392	Yes	0.330	2.4901
7	0.500	No	0.499	0.3057
8	0.500	Yes	0.468	2.4901
9	0.522	Yes	0.499	2.4901

precipitation in case 2 and 3 in comparison with case 1.

As shown in Fig. 8, in the very early stages of phase separation, the fraction of α' is higher in case 1 then that in cases 2 and 3, although this trend reverses soon. The curves for cases 2 and 3 also intersect after around 2.5×10^7 sec. since the average initial concentration is slightly lower in case 3 than that in case 2, the incubation time for nucleation is longer. On the contrary, since there is less precipitation in case 3, the

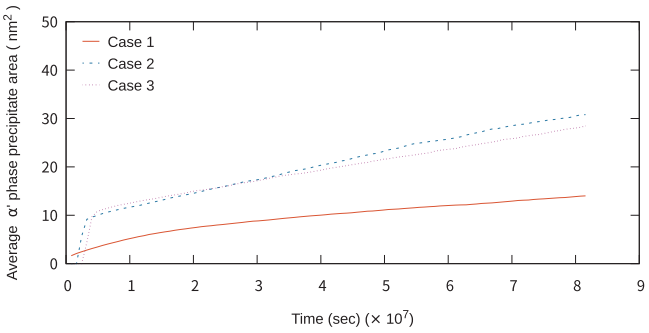

Fig. 8. Plots of average α' precipitate area for Cases 1,2 and 3 in Table 1.

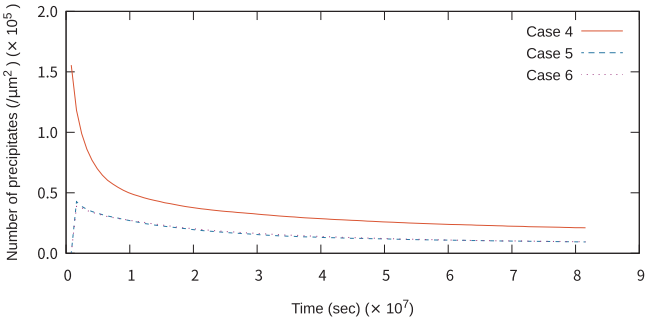

Fig. 9. Plots of number density of α' precipitates per unit area ($/\mu m^2$) for Cases 4,5 and 6 in Table 1.

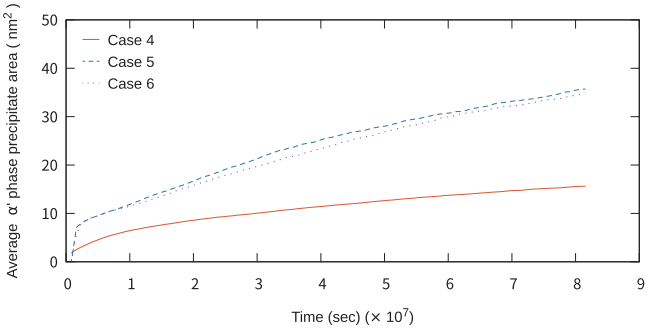

Fig. 10. Plots of average α' precipitate area for Cases 4,5 and 6 in Table 1.

average precipitate area is marginally larger during the transient regime ($0.5 \times 10^7 - 2.5 \times 10^7$ s), even though it later becomes larger in case 2. To check that this trend was consistent, we repeated the simulations with different random seeds. Since the α' phase fraction was consistently higher in case 5 then that in case 6, we were unable to observe any intersection between their curves (Fig. 10). We also found that the precipitate number density curves for cases 5 and 6 (Fig. 9) mostly overlapped, whereas the average initial concentration was higher in case 5 then that in case 6.

Miller et al. observed that the α' precipitates are mostly spherical at low Cr concentrations but become interconnected as the Cr concentration increased [4]. Our simulation results are consistent with this observation. When the average initial Cr concentration is greater than 0.5 in cases 7–9, the microstructure (Fig. 12) exhibits two distinct phases rather than being a mixture of matrix and precipitate, whereas the α' phase's morphology is mostly circular, as shown in Figs. 6 and 11. On the contrary, it exhibits an interconnected microstructure in Fig. 12. However, for the sake of terminological consistency, we still refer to closed α' regions as precipitates in Figs. 13 and 14.

In cases of 7–9, no intersections can be observed over time in either

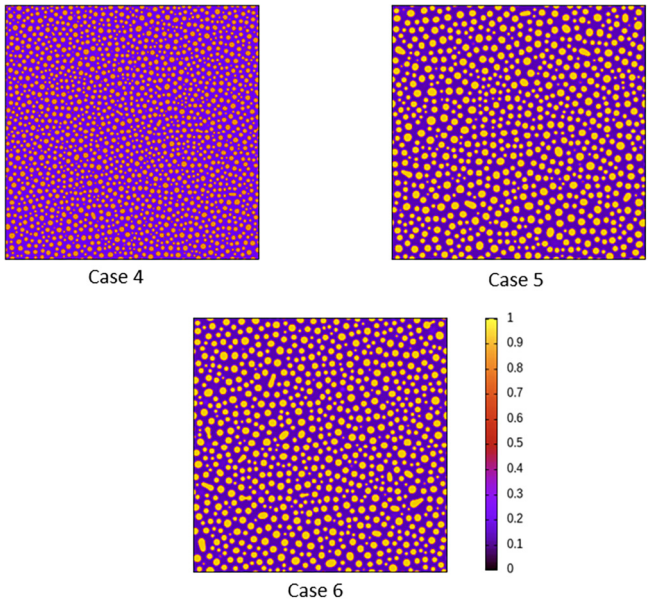

Fig. 11. Plots of Chromium concentration at $t = 8156.7\ s$ (1.0×10^6 time steps). Numbers of α' precipitates per μm^2 are 21080, 9389 and 9447 and the average precipitate areas are 15.63 nm^2, 35.68 nm^2 and 34.89 nm^2 for Cases 4,5 and 6, respectively.

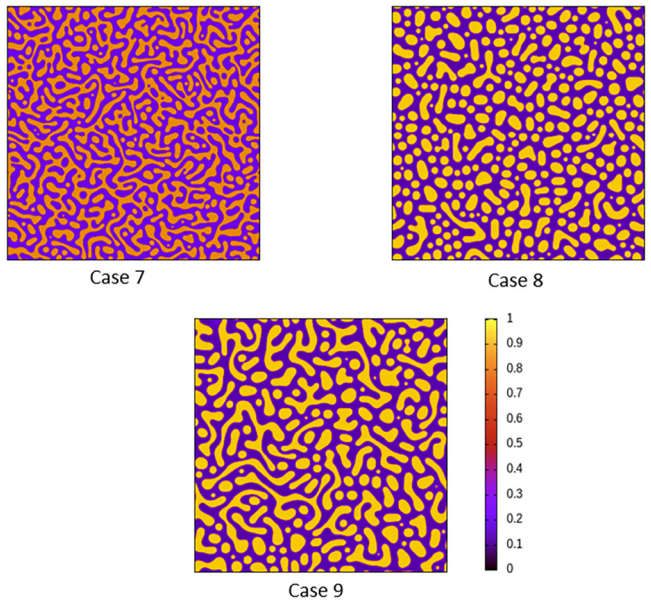

Fig. 12. Plots of Chromium concentration at $t = 8156.7\ s$ (1.0×10^6 time steps). Numbers of α' precipitates per μm^2 are 1578, 3905 and 1871 and the average precipitate areas are 315.99 nm^2, 119.88 nm^2 and 266.59 nm^2 for Cases 7,8 and 9, respectively.

the precipitate number density plot (Fig. 13) or the average precipitate area plot (Fig. 14). However, if we compare cases 8 and 9, we see significant differences in both the precipitate number density and average precipitate area in these figures. Also, even though the α' phase fractions in case 7 and 9 are the same (Fig. 12) and their precipitate number densities are comparable, the interconnected structures, as shown in Figs. 7 and 9, are noticeably different from each other. Therefore, we introduced another metric to quantitatively distinguish these structures.

As shown in Fig. 15, we draw auxiliary lines in four directions (up, down, and two diagonals) on the microstructure. Then, we converted the microstructure into a sharp interface representation where matrix

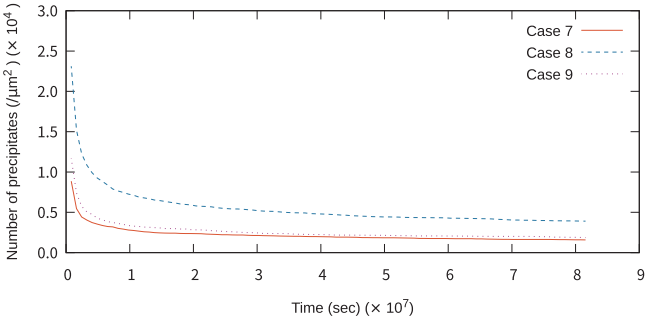

Fig. 13. Plots of number density of α' precipitates per unit area ($/\mu m^2$) for Cases 7,8 and 9 in Table 1.

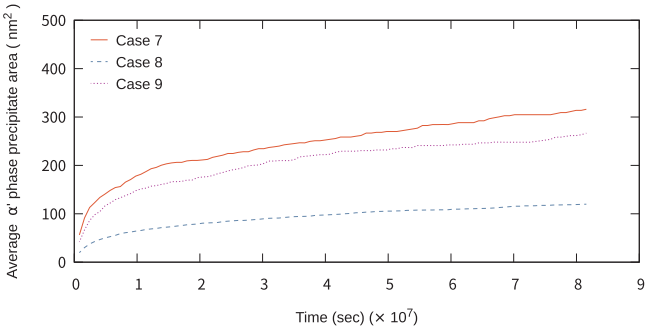

Fig. 14. Plots of average α' precipitate area for Cases 7,8 and 9 in Table 1.

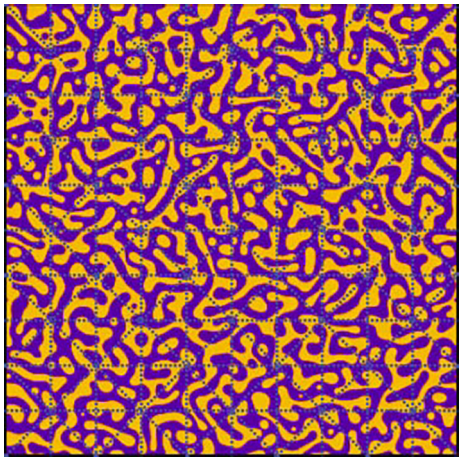

Fig. 15. Microstructure of Case 9 in Fig. 12 with auxiliary lines (blue dashed line). We counted number of voxels on the auxiliary lines to calculate summed number of phase boundaries along the line.

regions are assigned the values of 0 and α' precipitate regions are assigned positive integer values. Then, we count the number of transitions from 0 to a positive integer or vice versa along each of the auxiliary lines, summing the results for 10 lines in each direction and plotted the result in Fig. 16. Now, even though the α' phase fractions and precipitate number densities are comparable for case 7 and 9, we see significant differences in the numbers of phase boundaries along these lines with the phase boundary density being significantly higher in case 7 than that in case 9. This implies that the two microstructures may exhibit significant differences in the strengthening effect caused by hindering dislocation migration at phase boundaries.

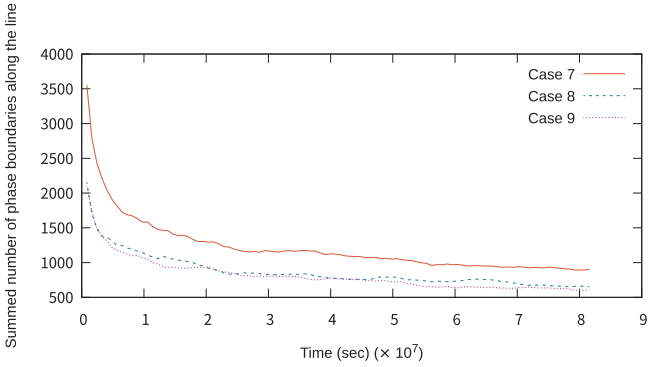

Fig. 16. Plots of summed number of phase boundaries along auxiliary lines in Fig. 15 for cases 7,8 and 9 in Table 1.

3. Conclusions

Herein, we simulated a set of phase-field models to investigate the phase separation behavior in the Fe-Cr binary alloy system. When the average initial concentration was between 0.377 and 0.400, magnetic ordering effects significantly increased the interfacial energy between the matrix and precipitated phases, reducing the number of precipitates while increasing the average precipitate area accordingly. On the contrary, when we compared two cases with average initial concentrations of 0.500 and 0.522, we found that the precipitate number density decreased significantly as the concentration increased, whereas the average precipitate area also decreased noticeably. When we compared two cases with average initial concentrations of 0.500 and 0.522, ignoring magnetic ordering effects in the former case but accounting for them in the latter, we found that their α' fractions and precipitate number densities were comparable. However, the density of phase boundaries along certain auxiliary lines depended significantly on the presence of magnetic ordering effects, which can noticeably affect matarial's mechanical properties.

Data availability

The raw/processed data required to reproduce these findings cannot be shared at this time as the data also forms part of an ongoing study.

Acknowledgments

This work was supported by a grant from Kyung Hee University in 2018 (KHU-20181165). This work has supported by the National Research Foundation of Korea (NRF) grant funded by the Korea government (MSIT) (NRF-2019M2D2A1A01032534).

References

[1] P. Grobner, The 885 f (475 c) embrittlement of ferritic stainless steels, Metall. Trans. 4 (1) (1973) 251–260.
[2] D. Chandra, L. Schwartz, Mössbauer effect study of the 475 c decomposition of fe-cr, Metall. Trans. 2 (2) (1971) 511–519.
[3] H. Solomon, L.M. Levinson, Mössbauer effect study of 475 c embrittlement'of duplex and ferritic stainless steels, Acta Metall. 26 (3) (1978) 429–442.
[4] M. Miller, J. Hyde, M. Hetherington, A. Cerezo, G. Smith, C. Elliott, Spinodal decomposition in fe-cr alloys: Experimental study at the atomic level and comparison with computer models-i. Introduction and methodology, Acta Metall. Mater. 43 (9) (1995) 3385–3401.
[5] Y.-S. Li, S.-X. Li, T.-Y. Zhang, Effect of dislocations on spinodal decomposition in fe–cr alloys, J. Nucl. Mater. 395 (1–3) (2009) 120–130.
[6] P. Hedström, S. Baghsheikhi, P. Liu, J. Odqvist, A phase-field and electron microscopy study of phase separation in fe–cr alloys, Mater. Sci. Eng.: A 534 (2012) 552–556.
[7] L. Zhu, Y. Li, C. Liu, S. Chen, S. Shi, S. Jin, Effect of applied strain on phase separation of fe–28 at.% cr alloy: 3d phase-field simulation, Modell. Simul. Mater. Sci. Eng. 26 (3) (2018) 035015.
[8] J. Lim, I.S. Hwang, J.H. Kim, Design of alumina forming fecral steels for lead or

lead–bismuth cooled fast reactors, J. Nucl. Mater. 441 (1–3) (2013) 650–660.
[9] O. Soriano-Vargas, E.O. Avila-Davila, V.M. Lopez-Hirata, N. Cayetano-Castro, J.L. Gonzalez-Velazquez, Effect of spinodal decomposition on the mechanical behavior of fe–cr alloys, Mater. Sci. Eng.: A 527 (12) (2010) 2910–2914.
[10] A. Dinsdale, Sgte data for pure elements, Calphad 15 (4) (1991) 317–425.
[11] C. Nvidia, Programming guide (2010).
[12] R. Chandra, L. Dagum, D. Kohr, R. Menon, D. Maydan, J. McDonald, Parallel Programming in OpenMP, Morgan kaufmann, 2001.
[13] J.W. Cahn, J.E. Hilliard, Free energy of a nonuniform system. I. Interfacial free energy, J. Chem. Phys. 28 (2) (1958) 258–267.
[14] L.Q. Chen, J. Shen, Applications of semi-implicit fourier-spectral method to phase field equations, Comput. Phys. Commun. 108 (2–3) (1998) 147–158.
[15] A. Yamanaka, T. Aoki, S. Ogawa, T. Takaki, Gpu-accelerated phase-field simulation of dendritic solidification in a binary alloy, J. Cryst. Growth 318 (1) (2011) 40–45.
[16] J. Hötzer, A. Reiter, H. Hierl, P. Steinmetz, M. Selzer, B. Nestler, The parallel multi-physics phase-field framework pace3d, J. Comput. Sci. 26 (2018) 1–12.
[17] J.W. Cahn, On spinodal decomposition, Acta Metall. 9 (9) (1961) 795–801.
[18] J.-O. Andersson, J. Ågren, Models for numerical treatment of multicomponent diffusion in simple phases, J. Appl. Phys. 72 (4) (1992) 1350–1355.
[19] R.R. Mohanty, J.E. Guyer, Y.H. Sohn, Diffusion under temperature gradient: a phase-field model study, J. Appl. Phys. 106 (3) (2009) 034912.
[20] J.-O. Andersson, B. Sundman, Thermodynamic properties of the cr- fe system, Calphad 11 (1) (1987) 83–92.
[21] M. Frigo, S.G. Johnson, Fftw user's manual, Massachusetts Institute of Technology.
[22] C. Nvidia, The cufft library user guide.
[23] D.A. Porter, K.E. Easterling, M. Sherif, Phase Transformations in Metals and Alloys (Revised Reprint), CRC Press, 2009.